Article

Development of a Pneumatically Actuated Quadruped Robot Using Soft-Rigid Hybrid Rotary Joints

Zhujin Jiang [1], **Yan Wang** [1] **and Ketao Zhang** [1,*]

[1] Advanced Robotics at Queen Mary (ARQ), School of Engineering and Materials Science, Queen Mary University of London, London, E1 4NS, UK; z.jiang@qmul.ac.uk; exx569@qmul.ac.uk; ketao.zhang@qmul.ac.uk

[*] Correspondence: ketao.zhang@qmul.ac.uk

Abstract: Inspired by the musculoskeletal systems in nature, this paper presents a pneumatically actuated quadruped robot consisting of a rectangular torso and four 2-degree of freedom (DoF) planar robot legs with soft-rigid hybrid rotary joints. We first introduce the mechanical design of the rotary joint and integrated quadruped robot with minimized onboard electronic components. Based on the unique design of the rotary joint, a joint-level PID-based controller is adopted to control the angular displacement of the hip and knee joints of the quadruped robot. Typical gait patterns for legged locomotion, including the walking and Trot gaits, are investigated and designed. Proof-of-concept prototypes of the rotary joint and quadruped robot are built and tested. Experimental results demonstrate that the rotary joint generates a maximum torque of 5.83 *Nm* and the quadruped robot is capable of locomotion with the trot gait at 187.5 *mm/s* and a frequency of 1.25 *Hz* and the walking gait at 12.8 *mm/s* and a gait cycle of 7.84 *s*. This study reveals that compared to soft-legged robots, the soft-rigid hybrid-legged robot has a simplified analytical model for motion control, scalability of size and high movement speed, thereby exhibiting significant potential for applications in extreme environments.

Keywords: quadruped robot; pneumatic actuation; soft-rigid hybrid structure; rotary joint; extreme environments.

1. Introduction

Working in extreme conditions, including explosive, nuclear, high-voltage and magnetic-resonance environments, is a big challenge for robots. Electric motor-driven robots have been extensively studied due to their efficiency, precision, versatility and adaptability [1], including the wheeled, tracked and legged robots that use electric motors as the primary power source to perform various tasks and functions. For example, the fully sealed wheeled robots [2-3] use electric motors to drive the wheels for operations in chemical, radiological and nuclear missions. However, the degree of confidence decreases over time as the sealed components show different responses to vibrations, temperature, etc. Besides, the tracked robots [4] relying on electrical motor-driven tracks have advantages over their wheeled counterparts in load tolerances and flexible mobility on soft, slippery and rough terrains without sinking. They have been developed for use in radioactive and hazardous environments [5] and offshore oil and gas platforms [6]. However, the operating time of these robots in radioactive conditions was limited by the maximum dose their weakest components could sustain. Compared to wheeled and tracked robots, electric motor-driven legged robots [1,7] have the ability to make and break contact with the ground, thus navigating on challenging terrains like rough and narrow spaces. They were built for applications in nuclear plants [8-9], oil/gas platforms

[10-11] and underground mines [12], but their electronic components are at high risk of being damaged in radiation-contaminated spaces. They could cause electrical sparks and disastrous ignition in explosive environments.

Soft-legged robots [13] powered by pneumatic actuators can be fabricated using flexible materials with minimized electronic components and exhibit excellent characteristics such as inherent compliance, good impact resistance, high energy-to-weight ratio, safety interaction with humans and adaptability to a variety of hostile environments. For example, the untethered soft robot [14] fabricated with silicone rubbers had the adaptability to harsh environmental conditions, including snowstorms, fires and water, although the locomotion speed is slow, only 0.0077 body length per second (*BL/s*). The soft quadruped robot with three degrees of freedom (DoFs) per leg [15] uses simple pneumatic oscillator circuits without any electronic components to generate walking gaits for operations in environments where electronics are not suitable, but these circuits are acted on additional control elements or based on manual input. The untethered hexapod robot in [16] with soft fluid-driven actuators composed of elastomer bladders enables complex deformations by leveraging viscous flows to produce non-uniform pressure between bladders to drive the robot to move in one direction at 0.05 *BL/s*. Further, soft-legged robots [17-19] are highly flexible, and their legs may exhibit other unwanted forms of deformation, such as radial and axial expansion due to the fabrication using soft materials, bringing challenges in kinematic model and motion control [20-21].

Aiming at addressing the challenges of electric motor-driven robots and soft-legged robots, pneumatically actuated soft-rigid hybrid-legged robots, also known as musculoskeletal robots [22-23] inspired by the musculoskeletal systems in nature [24-25], demonstrated promising capabilities in both building a precise kinematic model like electric motor-driven robots and adapting to various environments like soft-legged robots. For example, with the rigid exoskeleton providing structural support and the flexible pneumatic joints providing actuation and inherent mechanical compliance to absorb impact and improve safety in interactions with humans, soft-rigid hybrid bipedal robots [26], quadruped robots [27], hexapod robots [24] and arthropod-like robots [22] were proposed. These robots can achieve movement with simple gaits by manual input. Besides, despite the actuation delay and the decrease in actuator accuracy, the quadruped robots with antagonistic pneumatic actuators developed by Tsujita [28-29] achieved stable locomotion in walking and trot patterns by adopting an oscillator network controller and adjusting the stiffness at the trunk. The quadruped robots built by Fukuoka [30-31] can adapt to speed variation and stabilize the pace of running using a neuromorphic locomotion controller with leg loading feedback. However, human assistance was needed during experiments to avoid the possibility of falling over. Despite having great potential, soft-rigid hybrid-legged robots are a new trend in robotics and have not been thoroughly investigated [32]. One of the main limitations is that the development of legged robots using pneumatic actuators is complicated.

To further explore the potential of soft-rigid hybrid robots for operations in special environments, This paper proposes a soft-rigid hybrid rotary joint and develops a pneumatically actuated quadruped robot integrating a rectangular torso and four 2-DoF planar robot legs. The main contributions of this work include the mechanical design and experimental evaluation of a soft-rigid hybrid rotary joint, and the development of an integrated quadruped robot and its feasibility validation in typical gait control.

In the following sections, we first introduce the rotary joint design, quadruped robot integration, and controller development. The foot trajectories and typical gaits of the quadruped robot are also investigated. Following this process, section 3 presents the torque test of a single rotary joint and demonstrates the trot and walking gaits of the quadruped robot. Section 4 provides a detailed discussion of this work, and section 5 concludes the paper.

2. Development of the pneumatically actuated quadruped robot

2.1. Design of the soft-rigid hybrid rotary joint

The variable-stiffness actuators for soft robots have been developed by using antagonistic fluidic actuation [33]. For example, the theoretical models of the antagonistic rotary joints in [34-35] indicated that given an angular displacement/a torque, the torque/angular displacement is linear with the pressure difference between the two muscles, and the stiffness is related to the sum of pressures of the two muscles. However, the hinge function of the rotary joint in [34] may decline when the chambers are inflated to the fully deployed state for a long time. The maximum contraction ratio of the McKibben artificial muscle in [35] is only between 20% to 30%.

Inspired by the antagonistic fluidic actuation, we propose a soft-rigid hybrid rotary joint based on the twisting actuator developed in our previous work [36], as illustrated in Fig. 1. Two twisting skeletons are connected to the skeleton connector, where one performs a clockwise helical motion and another produces an anticlockwise helical motion. A soft bellows muscle is coupled to the twisting skeleton with a bearing and a bearing connector. The bellows muscle can be vacuumed and inflated, thereby generating linear driving force to actuate the twisting skeleton. The left end of twisting skeleton 1 is fixed to the end plate, while the right end of twisting skeleton 2 is connected to the output shaft. The outer ring of bearing 3 is fixed to the housing via a bearing cover. The linear motion of the output shaft is restricted by the inner ring of bearing 3 and the shaft sleeve. Therefore, the rotary joint generates pure rotation and torque at the output shaft by adjusting the pressures supplied to the two bellows muscles.
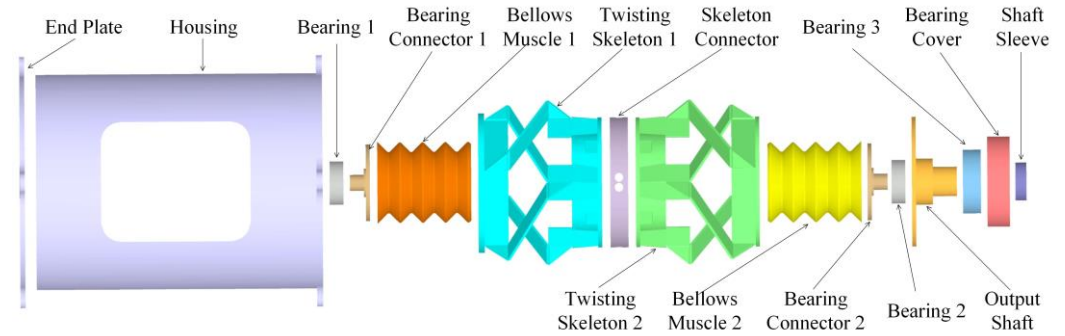

Figure 1. Exploded view of the soft-rigid hybrid rotary joint.

The two twisting skeletons of the rotary joint are illustrated in Fig. 2(a). The kinematic structure is shown in Fig. 2(b). The base, the middle platform and the upper platform are parallel and denoted by identical squares□$A_1B_1C_1D_1$, □$A_2B_2C_2D_2$ and □$A_3B_3C_3D_3$ with a radius of r, respectively. The angular displacement of the middle platform corresponding to the base of twisting skeleton 1 is denoted by θ_1. It can be measured between lines O_1B_1 and O_1Q_1 where Q_1 is the projection of vertex B_2 on the base. Besides, the link connecting the revolute joints R_{112} and R_{113} is denoted as L_{11} and its length is defined by the distance, l, between the two parallel joint axes. The length of the projection of L_{11} in the direction of O_1O_3 is denoted by h_1. Similarly, the angular displacement of the upper platform of twisting skeleton 2 is denoted by θ_2. It is measured between lines O_3B_3 and O_3Q_3 where Q_3 is the projection of vertex B_2 on the upper platform. The length of the projection of the link L_{21} connecting the revolute joints R_{212} and R_{213} in the direction of O_1O_3 is denoted by h_2. The angular displacement of the rotary joint defined as θ is calculated by
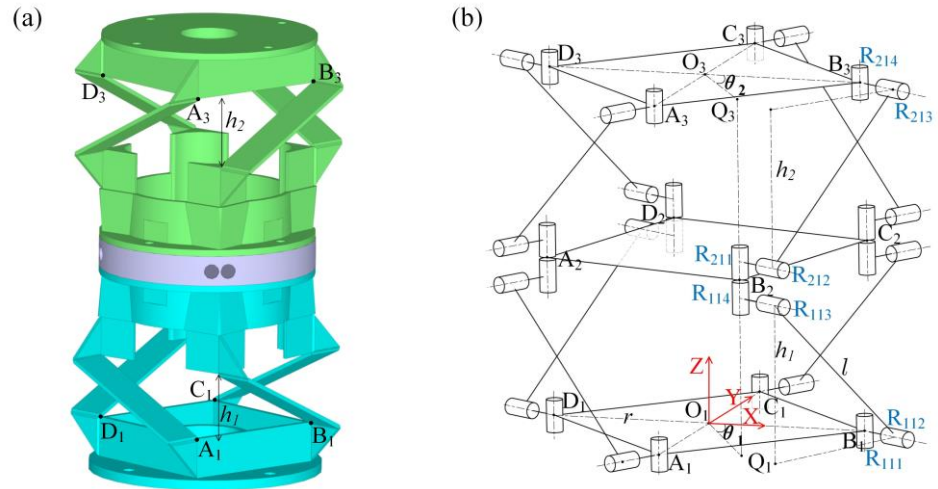
$$\theta = \theta_2 - \theta_1 \tag{1}$$

where

$$\sin\frac{\theta_i}{2} = \frac{\sqrt{l^2 - h_i^2}}{2r} \quad (i = 1, 2) \tag{2}$$

and the sum of h_1 and h_2 is constant.

Figure 2. (a) 3D model and (b) Kinematic structure of the twisting skeletons of the rotary joint.
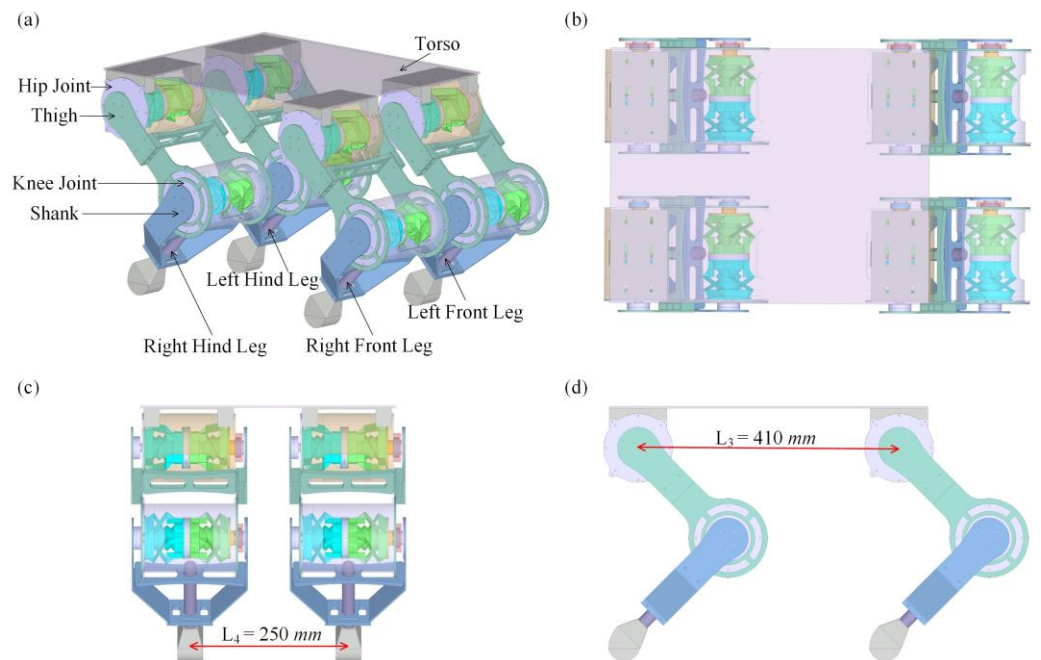
2.2. Integration of the quadruped robot

Using two rotary joints as the hip and keen joint, respectively, a planar 2-DoF robot leg is designed. The thigh consists of a beam and two plates where one plate connects the output shaft of the hip joint and the housing of the knee joint; another plate rotating freely around the hip joint provides structural support for the knee joint. The shank has a similar design to the thigh to support and drive the foot.

The quadruped robot consists of a torso and four 2-DoF robot legs, as shown in Fig. 3. The torso of the robot is a rigid rectangular plate. Four legs are fixed to the torso symmetrically. The design specification of the quadruped robot is listed in Tab. 1.

Figure 3. 3D design of the pneumatically actuated quadruped robot. (a) Isometric view. (b) Top view. (c) Left view. (d) Front view.

Table 1. Design specification of the quadruped robot

Length of the thigh L_1	200 *mm*
Length of the shank L_2	220 *mm*
Motion range of the hip joint β_1	[240°, 360°]
Motion range of the knee joint β_2	[210°, 330°]
Maximum torque of the hip joint	5.83 *Nm*
Maximum torque of the knee joint	5.83 *Nm*
Distance between front and rear legs L_3	410 *mm*
Distance between left and right legs L_4	250 *mm*
Weight of the robot leg	1080 *g*
Weight of the quadruped robot	5000 *g*

2.3. Controller for the soft-rigid hybrid rotary joint

The angular displacement of the rotary joint mainly depends on the pressure difference between the two bellows muscles due to the compliance of bellows muscles and flexure hinges of twisting skeletons. The larger the pressure difference is, the larger the angular displacement of the rotary joint is. Based on this characteristic, a joint-level PID-based controller is adopted to achieve the active angular displacement control, as shown in Fig. 4. Using the reference angular displacement θ_{ref} as the controller's input and the real-time angular displacement θ of the rotary joint as the feedback signal, the error between the reference angular displacement and the real-time angular displacement is calculated and transmitted to a PID module. The desired pressure difference ΔP is set as the output of the PID module. Combining the minimum pressure P_{min} which is directly set from an external port by users, the theoretical pressures P_1 and P_2 of the two bellows muscles are determined by Eqn. (3) and transferred to the pressure control units, which control the pressure supplied to the two bellows muscles of the rotary joint by using the pneumatic regulators and solenoid valves. In addition, the values of PID parameters are tuned manually by lifting the quadruped robot and evaluating the response of each joint to a step input, while P_{min} is set to 30 *kPa* for the robot's experiments.
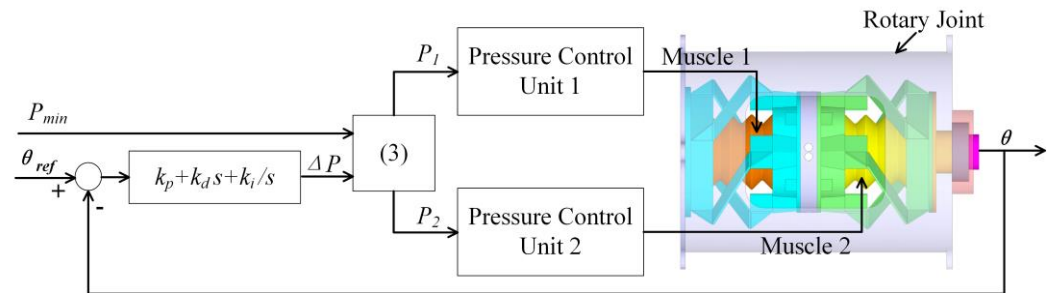

Figure 4. The PID-based controller of the rotary joint for the angular displacement control.

$$\begin{cases} P_1 = P_{\min}, \quad P_2 = P_{\min} - \Delta P \quad \text{if } \Delta P < 0 \\ P_2 = P_{\min}, \quad P_1 = P_{\min} + \Delta P \quad \text{if } \Delta P > 0 \end{cases} \tag{3}$$

2.4. Gait analysis

Quadruped robots can implement various gaits, such as crawling, walking, trot, pace, and bounding gaits, determining how the robot moves and interacts with the environment. The typical gaits are different in sequences, as is the duration that each leg is in contact with the ground.

To generate periodic gaits, the phase $\phi_i (\phi_i \in [0,1], i = 1,2,3$ and $4)$ is used to depict the state of each leg in a gait cycle, and the duty cycle is denoted by d $(d \in [0,1])$ to

represent the percentage of the gait cycle during which the leg is in contact with the ground. At the start of the gait cycle, each leg starts in stance with a phase of $\phi_i = 0$. The leg switches from the stance state to the swing state when ϕ_i increases to d. Once the phase ϕ_i increases to the maximum value of 1, it wraps around to zero, and the leg switches from the swing state back to the stance state, starting the next gait cycle. The phase of the *i*-th leg can be calculated by

$$\phi_i = \frac{t - t_{i,0}}{T} \tag{4}$$

where t is the current time; $t_{i,0}$ is the start time of the current gait cycle of the *i*-th leg; T is the period of one gait cycle. For higher velocity, a smaller gait period T is more suitable. With a constant gait period T, a smaller duty cycle d would result in each leg having an increased aerial time and create a more dynamic gait. Note that the four legs may have different values of $t_{i,0}$ and ϕ_i.

Besides, the phase offset $\theta_i (\theta_i \in [0,1], i = 1,2,3$ and $4)$ is defined to coordinate the phase ϕ_i of the *i*-th leg with respect to the phase ϕ_1 of the leading leg to produce different gait patterns through the relationship:

$$\phi_i = \phi_1 + \theta_i. \tag{5}$$

Table 2 lists the duty factor and desired phase offset for defining typical gaits, including the crawl, walking, trot, pace and bounding gaits. Based on the parameters given in Tab. 2, Fig. 5 lists the sequences of the leg movement with the trot and walking gaits. The solid blue color bars indicate the stance phase of the corresponding leg, while the white color bars represent the swing phase of the corresponding leg. In the trot gait, two diagonally opposite legs (e.g., the right front and left hind legs) are in contact with the ground while the other two legs are lifted and move forward. In the walking gait, a leg in the air is set down at the same instant as another leg is lifted, and three legs contact the ground at all times.

Table 2. The duty factor and desired phase offset of the typical gaits, including the crawl, walking, trot, pace and bounding gaits for the left hind leg (LH), left front leg (LF), right front leg (RF) and right hind leg (RH).

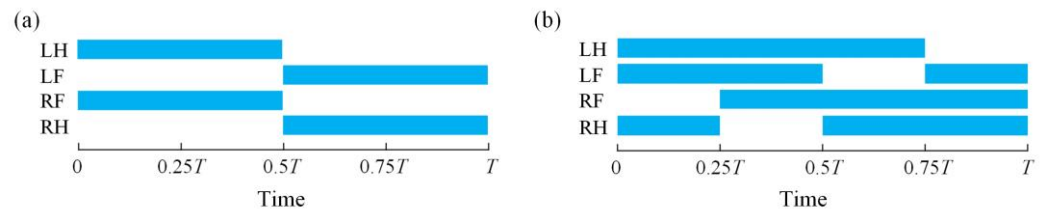| Gait	Duty Factor d	Phase Offset θ_i [LH, LF, RF, RH]
Crawl	0.8	[0, 0.75, 0.25, 0.5]
Walking	0.75	[0, 0.75, 0.25, 0.5]
Trot	0.5	[0, 0.5, 0, 0.5]
Pace	0.5	[0, 0, 0.5, 0.5]
Bounding	0.4	[0, 0.5, 0.5, 0]

Figure 5. Sequences of the leg movement with typical gaits in one gait cycle. (a) Trot gait. (b) Walking gait. The solid blue color bars indicate the stance phase of the corresponding leg while the white color bars represent the swing phase of the corresponding leg. (LH: the left hind leg; LF: the left front leg; RF: the right front leg; RH: the right hind leg.)

2.5. Foot trajectory

As illustrated in Fig. 6(a), a coordinate frame O_1-XYZ is set at the leg where the origin is located at the center of the hip joint O_1, the X-axis is horizontal, and the Y-axis is

vertical. Based on the Denavit–Hartenberg method, the position of the foot O_3 (x_3, y_3, z_3) expressed in the O_1−XYZ can be derived as

$$
O_3 = \begin{bmatrix} L_1\cos\beta_1 + L_2\cos(\beta_1 + \beta_2) \\ L_1\sin\beta_1 + L_2\sin(\beta_1 + \beta_2) \\ 0 \end{bmatrix} \tag{6}
$$

where L_1, L_2, β_1 and β_2 are the length of the thigh, the length of the shank, the angle of the hip joint and the angle of the knee joint, respectively. The inverse kinematics can be solved based on the conventional geometric approach. For a given position of the foot, the angles of the hip and knee joints are derived as

$$
\beta_1 = \text{atan2}\left(\frac{y_3}{x_3}\right) + \beta_3 + 2\pi \tag{7}
$$

$$
\beta_2 = \pi + \arccos\left(\frac{L_1^2 + L_2^2 - x_3^2 - y_3^2}{2L_1 L_2}\right) \tag{8}
$$

where

$$
\beta_3 = \arccos\left(\frac{x_3^2 + y_3^2 + L_1^2 - L_2^2}{2L_1\sqrt{x_3^2 + y_3^2}}\right) \tag{9}
$$

One gait cycle of the foot can be divided into a stance phase and a swing phase. To minimize the impact between the ground and the foot, the foot trajectory should meet the demand that the velocity and acceleration of the foot along the direction of the Y-axis (Fig. 6(a)) become zero at the time of touchdown, liftoff and maximum foot height [37]. Besides, the legs support the torso to move forward during the stance phase. To make the torso move steadily, the acceleration of the foot along the direction of the X-axis shown in Fig. 6(a) needs to be as small as possible. Therefore, the foot trajectory in the swing phase can be composed of a cubic curve along the X-direction and a cosine curve along the Y-direction, while the foot trajectory in the stance phase can be a straight line along the X-direction [38]. The equations for defining the foot trajectory with respect to the coordinate frame O_1−XYZ set at the center of the hip joint are:

$$
x_{st}(t_1) = L_s \times \left(\frac{1}{2} - \frac{t_1}{dT}\right) + L_t, \quad t_1 \in [0, dT] \tag{10}
$$

$$
y_{st}(t_1) = -H_t, \quad t_1 \in [0, dT] \tag{11}
$$

$$
x_{sw}(t_1) = \frac{L_s}{2} \times \left(-64s^3 + 144s^2 - 100s + 21\right) + L_t, \quad t_1 \in [dT, T] \tag{12}
$$

$$
y_{sw}(t_1) = -H_t + H_f \times \frac{1 - \cos(4\pi s)}{2}, \quad t_1 \in [dT, T] \tag{13}
$$

where

$$
s = \left(\frac{t_1}{T} - d\right) \times \frac{1}{2(1-d)} + \frac{1}{2} \tag{14}
$$

L_s denotes the stride length; t_1 represents the remainder of the real-time divided by the gait cycle T; L_t denotes the distance between the axis of symmetry of the foot trajectory and the hip joint; H_t and H_f represent the height of the hip joint and the maximum height of the foot in the Y-axis with respect to the ground, respectively. Equations (10) and (11) represent the position variation of the foot along the X- and Y-axes during the stance phase, respectively, while Eqs. (12) and (13) represent its position variation along the X- and Y-axes during the swing phase, respectively.

To evaluate the dynamic performance of the quadruped robot, trot and walking gaits are chosen for experiments. The parameters $T = 0.8$ *s*, $H_t = 297$ *mm*, $H_f = 70$ *mm*, $L_s = 150$ *mm* and $L_t = 0$ *mm* are set for the trot gait. Figure 6(b) shows the foot trajectory of the

quadruped robot with the trot gait, while Figs. 6(c) and 6(d) illustrate the theoretical angular displacements of the hip and knee joints of the quadruped robot with the trot gait, respectively. (The angular displacements of 0° in Figs. 6(c) and 6(d) are corresponding to $\beta_1 = 315°$ and $\beta_2 = 270°$ shown in Fig. 6(a), respectively.) By contrast, the parameters T = 7.84 *s*, H_t = 285 *mm*, H_f = 80 *mm*, L_s = 100 *mm* and L_t = 50 *mm* are set for the walking gait. Figs. 7(a) and 7(b) illustrate the theoretical angular displacements of the hip and knee joints of the quadruped robot with the walking gait, respectively.
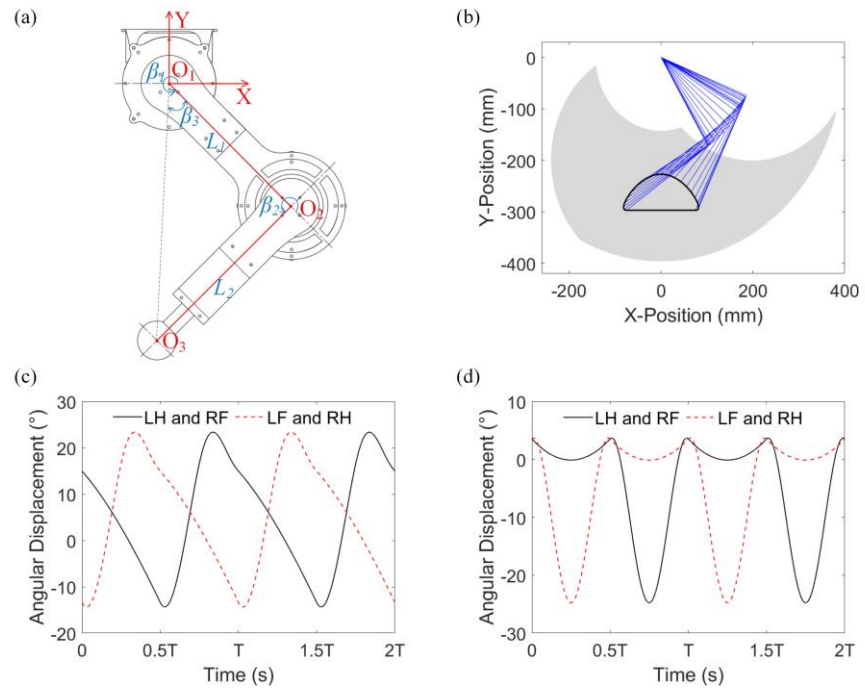

Figure 6. Leg movement of the quadruped robot with the trot gait. (a) Schematic diagram of the 2-DoF robot leg. (b) Foot trajectory of the quadruped robot with the trot gait. (c) Angular displacement of the hip joints of the quadruped robot with the trot gait. (d) Angular displacement of the knee joints of the quadruped robot with the trot gait. (LH: the left hind leg; LF: the left front leg; RF: the right front leg; RH: the right hind leg.)
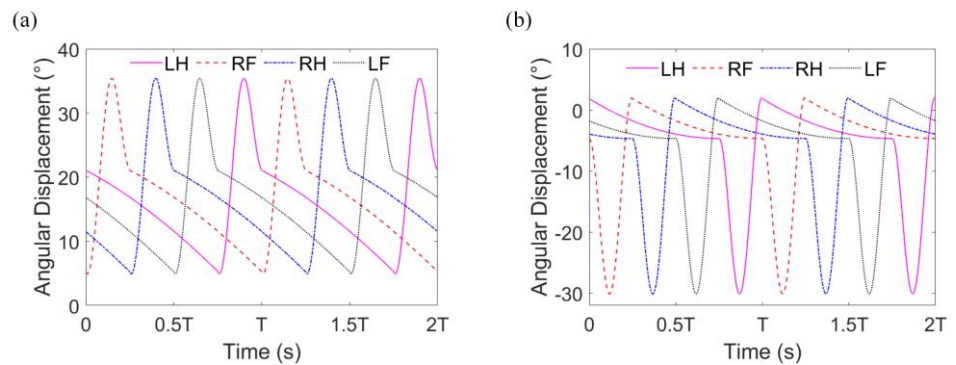

Figure 7. Leg movement of the quadruped robot with the walking gait. (a) Angular displacement of the hip joints of the quadruped robot with the walking gait. (b) Angular displacement of the knee joints of the quadruped robot with the walking gait. (LH: the left hind leg; LF: the left front leg; RF: the right front leg; RH: the right hind leg.)
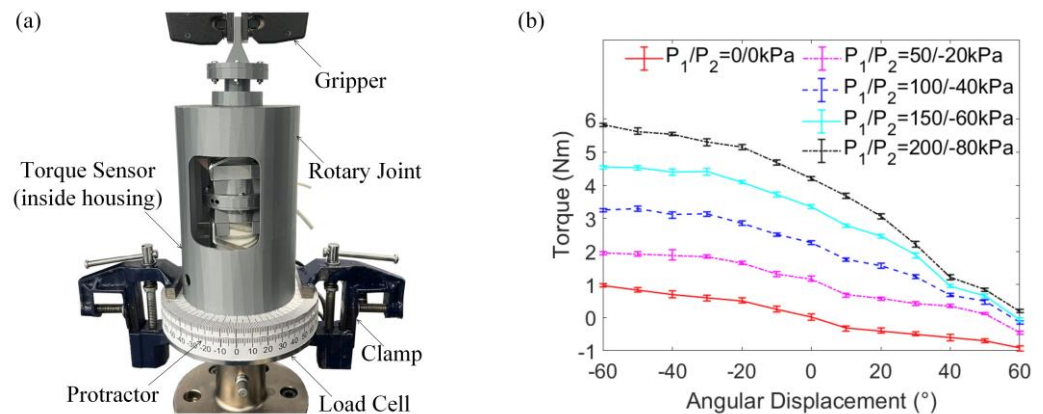
3. Experimental evaluation of the rotary joint and integrated quadruped robot

To evaluate the performances, prototypes of the rotary joint and quadruped robot are fabricated using 3D printing and CNC approaches to achieve rapid and low-cost manufacturing. TPU 95A filament is selected as the material for printing the soft bellows

muscles of the rotary joint due to its exceptional wear and tear resistance and rubber-like flexibility. The thighs, shanks and housings of the rotary joints are 3D-printed with the PLA material. The twisting skeletons of the rotary joints are CNC-machined using multi-layered aluminium composite panels (HYLITE) with a polypropylene core and aluminium cover layers, which have good fatigue resistance and can provide a compliant hinge function to withstand repeated bending without damage. The feet are fabricated by injecting Dragon Skin 30 into prefabricated molds. The torso is cut with a carbon fiber plate. The quadruped robot prototype is obtained by assembling the modularized rotary joints and aforementioned components.

3.1. Torque evaluation of the soft-rigid hybrid rotary joint

Figure 8(a) illustrates the prototype of the rotary joint and experimental settings for evaluating its output torque. The base of the rotary joint is mounted on the load cell of the Instron machine E5967 by using two clamps, while the output shaft of the rotary joint is fixed to the gripper of the Instron machine. A 6-axis torque-force sensor (RO-BOTOUS RFT40-SA01) is installed between the twisting skeletons and the base of the rotary joint to measure its output torque.

Figure 8. Torque evaluation of the soft-rigid hybrid rotary joint. (a) Testing platform. (b) Output torque of the rotary joint.

The output torque of the rotary joint is tested by fixing the rotary joint and maintaining the bellows muscles at constant pressures. As the rotary joint is symmetric, the case of $P_1 \geq 0$ and $P_2 \leq 0$ is evaluated in this work. The experimental results in Fig. 8(b) reveal that without actuating the two bellows muscles ($P_1 = P_2 = 0$ kPa), the absolute value of the output torque increases when the rotary joint deviates from its initial position $\theta = 0°$, which results from the compliance of the bellows muscles and flexure hinges of the twisting skeletons. Given a certain angular displacement, increasing the pressure of bellows muscle 1 from 0 to 200 kPa and decreasing the pressure of bellows muscle 2 from 0 to -80 kPa leads to increased torque of the rotary joint, but the torque change of the rotary joint at the angular displacement $\theta > 0°$ is lower than that at the angular displacement $\theta < 0°$. The reason is when the angular displacement increases from 0° ($\theta > 0°$), bellows muscle 1 is extended, and its contact area with twisting skeleton 1 decreases; bellows muscle 2 is contracted, and its inner space decreases; inflating bellows muscle 1 and vacuuming bellow muscle 2 at the angular displacement $\theta > 0°$ generates a lower force than that the at the angular displacement $\theta < 0°$ to driving twisting skeletons. Further, The rotary joint is capable of generating a maximum torque of 5.83 Nm under the conditions of $\theta = -60°$, $P_1 = 200$ kPa and $P_2 = -80$ kPa.

3.2. System integration

The quadruped robot is tethered, and the pneumatic and control systems are off-board to reduce the weight of the quadruped robot. The PID-based controller is adopted for the rotary joints to achieve the active angular displacement control, which was developed using Matlab® on a desktop computer. The bellows muscles of the rotary joints are capable of being both inflated and vacuumed, and their pressures are adjusted by the pneumatic system which is composed of an air compressor, pneumatic regulators (SMC ITV-212BL4), three-port solenoid valves (SMC VDW350-5G-4-02F-Q), two-port solenoid valves (SMC VX220AGA) and vacuum generators (SMC ZH07DSA-06-06-06), as shown in Fig. 9. The data acquisition device (NI USB-6343) is connected to the computer for transmitting control commands from the controller to corresponding valves. The data acquisition device directly controls the pneumatic regulators via analogue output, while the two-port and three-port solenoid valves are driven by motor driver controllers L298N. (When receiving digital signals from the data acquisition device, the motor driver controller L298N generates analogue signals to control the solenoid valves.) Markers are attached to the thigh and the shank of each leg to measure the angular displacements of the hip and knee joints via the OptiTrack motion capture system, respectively. This information is fed back to the controller to realize the closed-loop control of the posture of the quadruped robot.
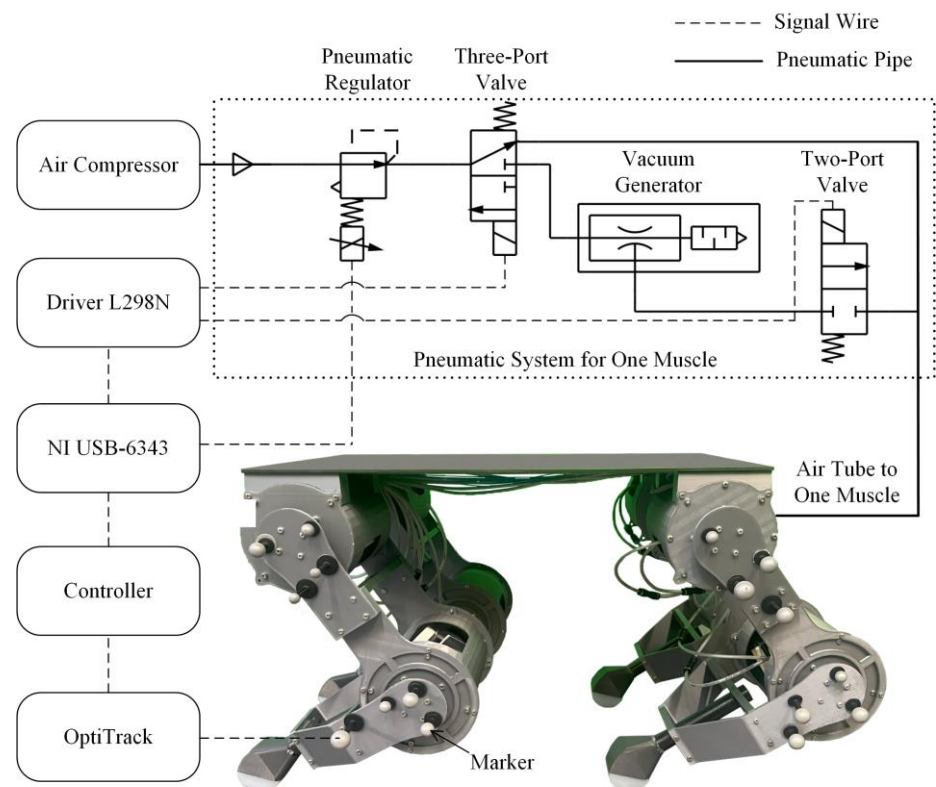

Figure 9. Pneumatic and control systems of the quadruped robot.

3.3. Trot gait test of the quadruped robot

To prevent the quadruped robot from falling sideways during tests, one end of a linkage connects the torso of the quadruped robot with a revolute joint, and another end of the linkage connects a guide carriage with a revolute joint. The guide carriage has one DoF and is capable of moving on the guide rail. Besides, to prevent the quadruped robot from radically rolling forward and backwards, the torso of the quadruped robot is also connected to strings. Another end of the strings is tied to a linear guide block, which can move along the linear slide rail. Using the theoretical trajectories shown in Figs. 6(c) and
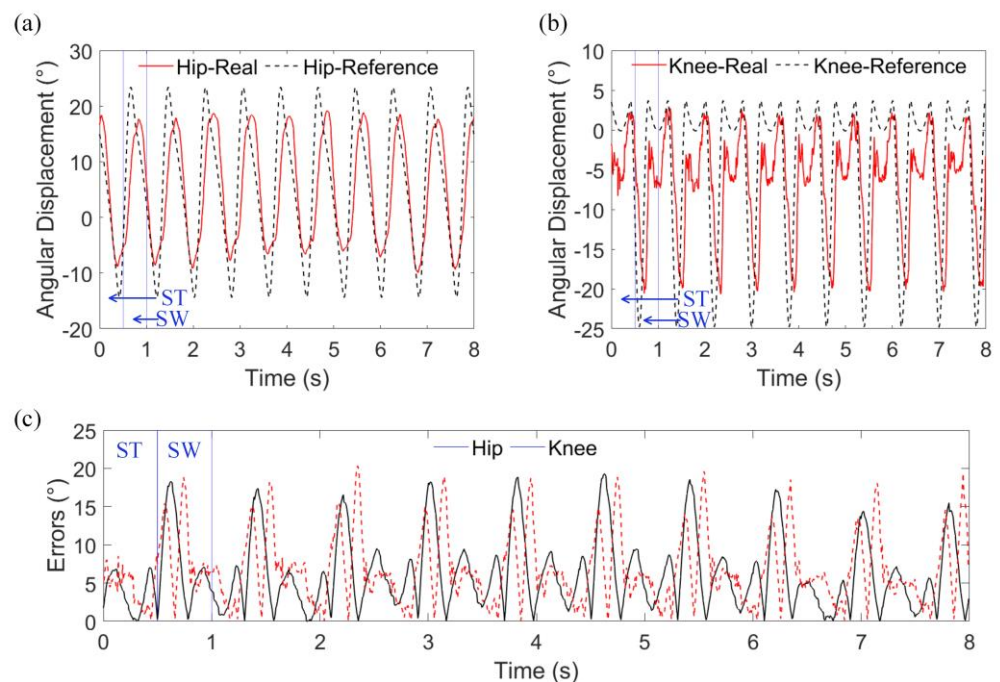
6(d) as inputs, the trot gait of the quadruped robot at 187.5 *mm/s* (0.36 *BL/s*) and a frequency of 1.25 *Hz* is tested on a treadmill (Supplementary Video S1). As illustrated in Fig. 10, the moving sequences of the quadruped robot with the trot gait are left front and right hind legs lift synchronously - left hind and right front legs lift synchronously - left front and right hind legs lift synchronously, which matches the sequences depicted in Tab. 2 and Fig. 5(a). As we control the position instead of the torque of supporting legs in the stance phase in the experiments, the elastic properties of robot legs are not fully explored and the strings connecting the quadruped robot are constantly under tension.
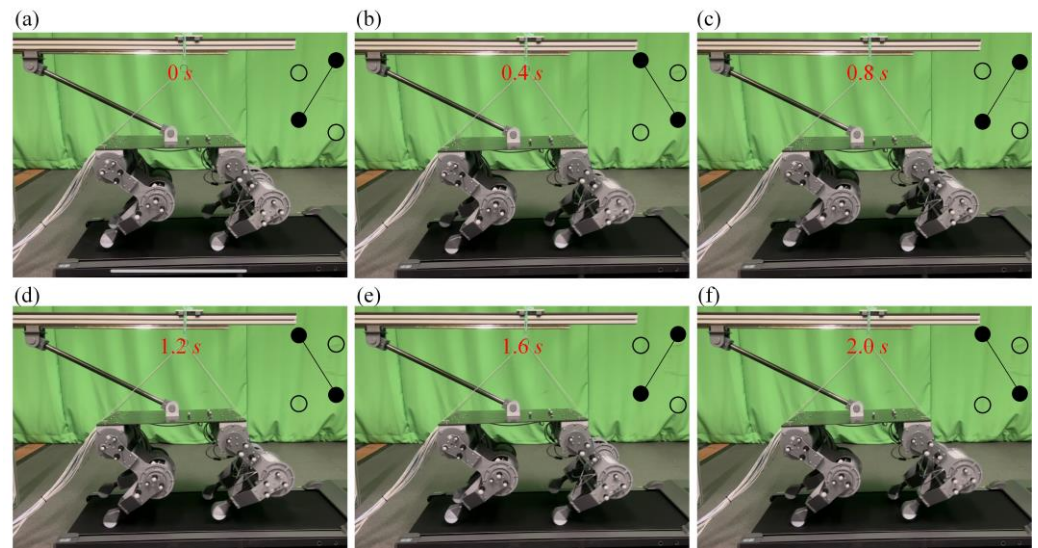
Figure 10. Moving sequences of the four legs of the quadruped robot with the trot gait. Solid circles denote the feet in ground contact. White circles denote lifting feet.

Figure 11. Movement of the left hind leg of the quadruped robot with the trot gait. (a) Angular displacement of the hip joint of the left hind leg. (b) Angular displacement of the knee joint of the left hind leg. (c) Errors of the angular displacements of the hip and knee joints of the left hind leg. (ST: stance phase; SW: swing phase.)

Further, as the movements of the four legs of the quadruped robot with the periodic trot gait are similar, the left hind leg is selected for analysis. The angular displacements of the hip and knee joints of the left hind leg with the trot gait in Figs. 11(a) and 11(b) illustrate that both the hip and knee joints of the left hind leg closely follow the reference trajectories. The errors of angular displacements of the hip and knee joints are depicted in Fig. 11(c). It shows that the error in the swing phase is significantly larger than that in the stance phase because the swing legs freely move in the air without any restrict from the ground, and other factors such as the sharp changes of the reference trajectories and the delay of the pneumatic pressure supply also negatively affect the results. In spite of the errors, Fig. 10 and Supplementary Video S1 demonstrate the quadruped robot is capable of smooth locomotion with the trot gait.

3.4. Walking gait test of the quadruped robot

Setting the theoretical trajectories shown in Figs. 7(a) and 7(b) as inputs, the walking gait of the quadruped robot at 12.8 *mm/s* and a gait cycle of 7.84 *s* is tested without using the treadmill (Supplementary Video S1). As illustrated in Fig. 12, the moving sequences of the quadruped robot with the walking gait are left front leg lift - left hind leg lift - right front leg lift - right hind leg lift - left front leg lift, which matches the sequences depicted in Tab. 2 and Fig. 5(b). The Supplementary Video S1 illustrates that the robot legs sometimes slip when they lift off (switch from the stance phase to the swing phase). This is because only a set of PID parameters is used to control the angular displacements of the hip and knee joints of the quadruped robot. (The robot in [32] was able to move without assistance by using two sets of PID parameters to control the leg in the swing phase and the stance phase, respectively, but its movement was clumsy.) Besides, to minimize the impact between the ground and the foot, the velocity and acceleration of the foot along the direction of the Y-axis are set to zero at the time of liftoff, so the foot does not generate a high force to kick the ground.
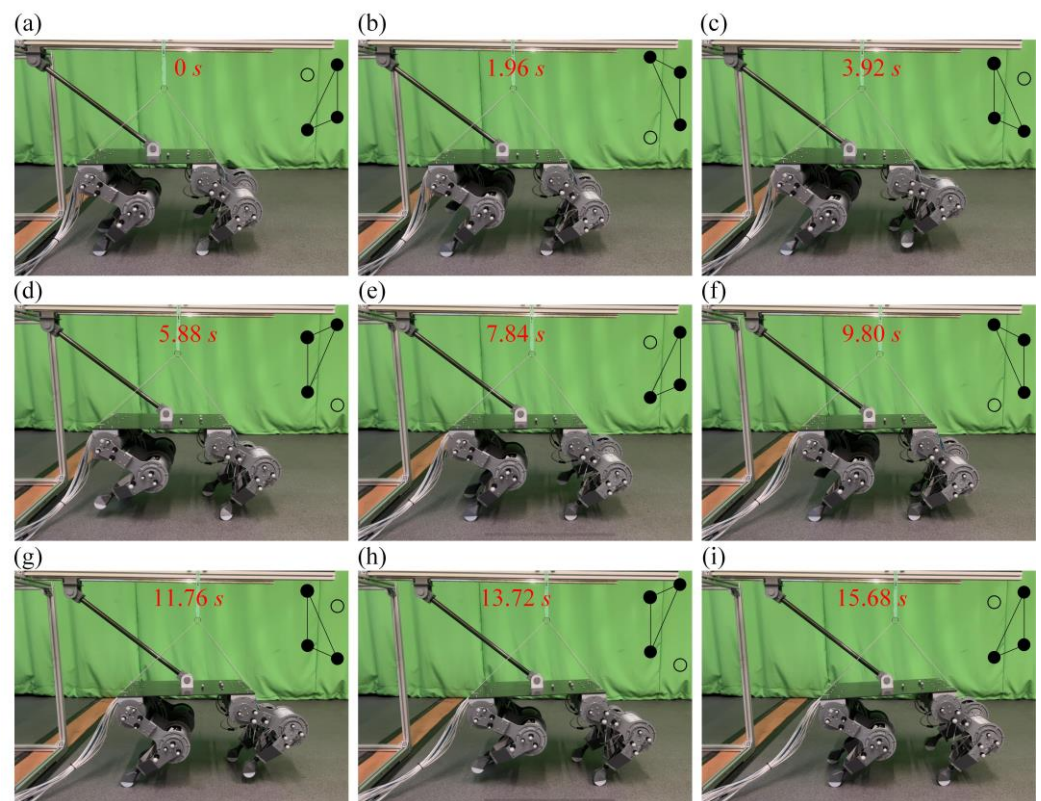

Figure 12. Moving sequences of the four legs of the quadruped robot with the walking gait. Solid circles denote the feet in ground contact. White circles denote lifting legs.

Similar to the trot gait test, the left hind leg is selected for tracking performance analysis. The angular displacements of the hip and knee joints of the left hind leg with the walking gait in Figs. 13(a) and 13(b) illustrate that both the hip and knee joints of the left hind leg are able to follow the reference trajectories. Figure 13(c) depicts that the errors of the hip and knee joints mainly occur at the peaks and troughs of reference trajectories in the swing phase, which are caused by the sharp changes of inputs and the actuation delay.
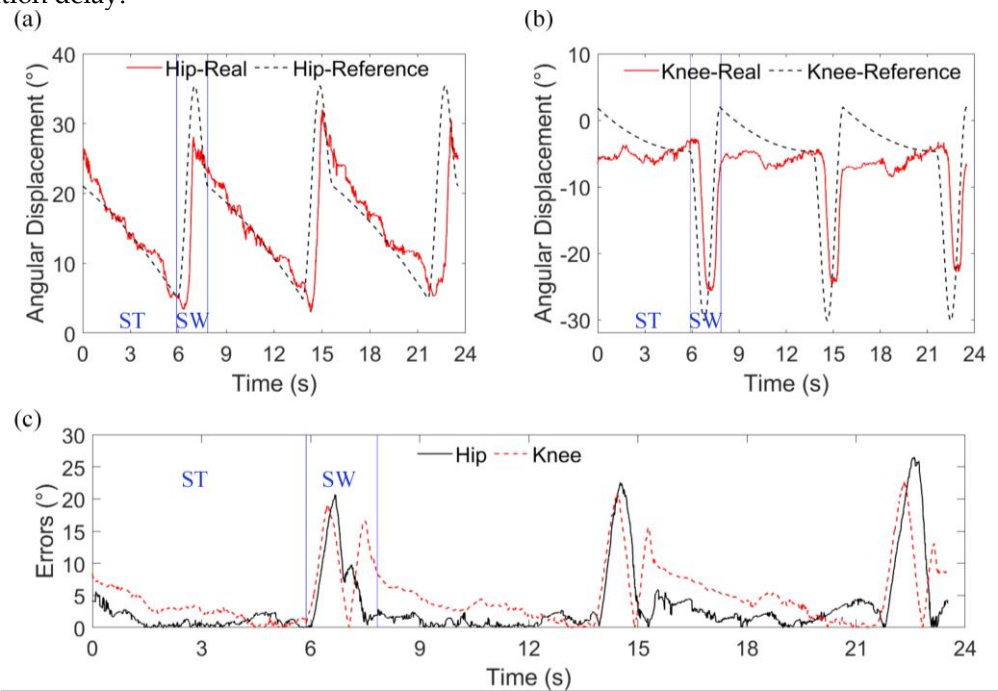

Figure 13. Movement of the left hind leg of the quadruped robot with the walking gait. (a) Angular displacement of the hip joint of the left hind leg. (b) Angular displacement of the knee joint of the left hind leg. (c) Errors of the angular displacements of the hip and knee joints of the left hind leg. (ST: stance phase; SW: swing phase.)

Table 3. Comparison of the quadruped robot with existing soft and soft-rigid hybrid robots.

Robots	Type	Speed (*BL/s*)	Advantages	Limitations
Proposed robot	Soft-rigid hybrid	0.36	High locomotion speed, compact structure, simplified modeling.	Difficulty in controller development for torque and stiffness control.
Untethered robot [14]	Soft	0.0077	Adaptability to adverse environments, including water and fire.	Slow locomotion speed, difficulty in kinematic modeling.
Hexapod robot [16]	Soft	0.05	2D workspace of the feet.	Movement in one direction, difficulty in kinematic modeling.
Multigait robot [17]	Soft	0.053	Simple design and control to generate mobility.	Difficulties in predictive modeling and motion control.
Modular robot [19]	Soft	0.033	Capable of translational motion and rotation.	Low motion accuracy.
Hexapod robot [22]	Soft-rigid hybrid	Around 0.26	Simplicity, lightweight, scalability.	Lack of sufficient traction, difficulty in controlling elastomeric balloons.
Walking robot [27]	Soft-rigid hybrid	0.05	No need for complex valves or bulky tethers.	Preprogrammed by hardware, difficult to move on rough surfaces.
Quadruped robot [31]	Soft-rigid hybrid	Around 1.2	Adaption to speed variation, stable pace running.	Complicated structure.

Further, Tab. 3 reveals that the proposed quadruped robot has a more simplified kinematic model for motion control and is capable of higher locomotion speed than soft-legged robots. Besides, compared to existing soft-rigid hybrid legged robots, the locomotion speed of the proposed quadruped robot is competitive, only slower than the soft-rigid hybrid-legged robot driven by McKibben-type pneumatic artificial muscles [31]. However, the McKibben-based robot is complicated since one leg has three joints with two external muscles actuating each joint; the distribution of McKibben artificial muscles needs to be specifically designed; and the robot's initial configuration is complex to be adjusted. By contrast, using the rotary joint with embedded pneumatic muscles as a module, the quadruped robot developed in this paper has a concise and compact structure and can be quickly adjusted.

4. Discussions

In this paper, a gait generator is used to generate typical gaits to coordinate the movement sequences of different legs, and a joint-level PID-based controller is adopted to control the angular displacements of the hip and knee joints of the quadruped robot. The feasibility of the quadruped robot in gait control is demonstrated, although preliminary experiments illustrate that the quadruped robot slips sometimes, exhibits large tracking errors in the swing phase and needs assistance during movement, including the linkage and strings presented in section 3.3. To eliminate the undesirable oscillatory behavior and realize stable movements of the quadruped robot without any assistance, control strategies such as the active model-based control [39], the adaptive fuzzy sliding mode control [40] and the reinforcement learning-based control [41] for predicting the unknown disturbance and improving the tracking performance of pneumatic artificial muscles with uncertainty and a considerable delay in characteristics will be further investigated. Besides, the advanced controllers used in electrical motor-driven robots like the torque control in adjusting the ground reaction force of supporting legs [42], and the closed-loop central pattern generator in leveraging compliance of elastic legs [43] could be considered for controlling the pneumatically actuated quadruped robot in the future.

Besides, variable stiffness is an essential characteristic of robots for safe physical human-robot interaction and adaptation to various environments and applications [44]. The variable-stiffness actuators for rigid-bodied robots have been developed by connecting motors to adjustable springs [45-46] or by building virtual controllers for motors [47-48] or by combining both [49]. In contrast, the variable-stiffness actuators for soft robots can be developed by using a pair of antagonistic muscles [33]. For example, the rotary joints reported in [34-35] have variable stiffness, which can be adjusted by controlling the internal pressures of the two antagonistic muscles without changing their position. The proposed rotary joint with two antagonistic bellows muscles has a similar arrangement to [34-35], and our previous work in [50] demonstrated that the bellows muscle is equivalent to a non-linear spring and the muscle can adjust its stiffness by changing its internal pressure. Hence, the proposed rotary joint has the potential of variable stiffness. How to derive the theoretical model of the output torque and stiffness of the proposed rotary joint and make use of it for highly dynamic motions of the quadruped robot will be explored in our future work.

It is worth to mention that pneumatic actuating systems composed of the air compressor, regulators and solenoid valves are normally heavy and bulky. Like most pneumatically actuated robots [27-32], in this work the pneumatic actuation system is off-board and the robot is tethered to make the robot lightweight. Though pneumatic robots without any external power source have recently been developed as reported in the references [14,15], the lightweight mini air compressors and valves bring in additional challenges, including the small volume of compressed gas, low flow rate, limited operating pressure and imprecise pressure control. Besides, the maximum output torque of the rotary joint used for the quadruped robot depends on its maximum operating pressure of 250 *kPa*, which is determined by the material selection and fabrication ap-

proach. By contrast, the maximum pressures of pneumatically actuated robots are 110 *kPa* in [20], 152 *kPa* in [14], 170 *kPa* in [15] and 400 *kPa* in [30-31], respectively. How to improve the airtightness and durability of the bellows muscle used in this paper is worth investigating.

Further, experiments in section 3 show that the quadruped robot is capable of moving with the trot gait at 187.5 *mm/s* and a frequency of 1.25 *Hz*. Compared to existing electrical motor-driven robots [51], the moving speed of the proposed quadruped robot is relatively low, which is limited to some extent by the weight of the legs. This can be improved by concentrating all rotary joints at the torso and actuating the knee joints with cables. For example, ScarlETH robot [42] uses chain and cable pulley systems to locate actuators directly at the hip joints to facilitate fast leg motion and reduce the energy losses in impact collisions. MIT Cheetah [52] actuates the knee joints through a parallel linkage, thereby minimizing the mass and inertia of the legs and maximizing impact mitigation. Similar designs will be considered in our later research.

5. Conclusions

This study developed a soft-rigid hybrid rotary joint and an evolved quadruped robot with a torso and four 2-DoF planar robot legs. With CNC-machined twisting skeletons using aluminium composite panels and 3D-printed bellows muscles using TPU 95A material, the rotary joint can generate a maximum torque of 5.83 *Nm*. By using a simplified PID-based controller to coordinate the angular displacements of hip and knee joints, the quadruped robot's feasibility in typical gait control were evaluated. Experimental results demonstrated that the quadruped robot is capable of movement with the trot gait at 187.5 *mm/s* (0.36 *BL/s*) and a frequency of 1.25 *Hz* and the walking gait at 12.8 *mm/s* and a gait cycle of 7.84 *s*. The quadruped robot has a more simplified kinematic model for motion control and is capable of higher movement speed than soft-legged robots. It also has a more compact and concise structure with pneumatic muscles embedded into rotary joints, and its configuration is easier to adjust compared to existing soft-rigid hybrid-legged robots driven by McKibben pneumatic artificial muscles, as given in Tab. 3. Further, this study paved the way to developing soft-rigid hybrid-legged robots with minimized onboard electronics for applications in environments where electrical motor-driven robots may not be suitable, such as in nuclear, explosive, and magnetic-resonance environments.

Author Contributions: Conceptualization, Z.J. and K.Z.; methodology, Z.J. and K.Z.; validation, Z.J. and Y.W.; formal analysis, Z.J.; writing—original draft preparation, Z.J.; writing—review and editing, K.Z.; funding acquisition, K.Z. All authors have read and agreed to the published version of the manuscript.

Data Availability Statement: The data used to support the findings of this study are available from the corresponding author upon request.

Conflicts of Interest: The authors declare that they have no conflicts of interest.

References

1. Taheri, H.; Mozayani, N. A study on quadruped mobile robots. *Mech. Mach. Theory.* **(2023)**, 190, 105448.

2. Guzman, R.; Navarro, R.; Ferre, J.; Moreno, M. Rescuer: Development of a modular chemical, biological, radiological, and nuclear robot for intervention, sampling, and situation awareness. *J. Field Robot.* **(2016)**, 33, 931-945.

3. Kawatsuma, S.; Fukushima, M.; Okada, T. Emergency response by robots to Fukushima‐Daiichi accident: summary and lessons learned. *Ind. rob. int.* **(2012)**, 39, 428-435.

4. Tibrea, S.; Nance, T.; Kriikku, E. Robotics in hazardous environments-real deployments by the savannah river national lab. *J.S.C. acad. sci.* **(2011)**, 9, 5.

5. Ducros, C.; Hauser, G.; Mahjoubi, N.; Girones, P.; Boisset, L.; Sorin, A.; Jonquet, E.; Falciola, J.M.; Benhamou, A. RICA: A tracked robot for sampling and radiological characterization in the nuclear field. *J. Field Robot.* **(2017)**, 34, 583-599.

6. Bogue, R. Robots in the offshore oil and gas industries: a review of recent developments. *Ind. Rob. Int. J. Robot. Res. Appl.* **(2020)**, 47, 1-6.

7. Biswal, P.; Mohanty, P.K. Development of quadruped walking robots: A review. *Ain Shams Eng. J.* **(2021)**, 12, 2017-2031.

8. Byrd, J.S.; Devries, K.R. A six-legged telerobot for nuclear applications development. *Int. J. Robot. Res.* **(1990)**, 9, 43-52.

9. Jang, Y.; Seol, W.; Lee, K.; Kim, K.S.; Kim, S. Development of quadruped robot for inspection of underground pipelines in nuclear power plants. *Electron. Lett.* **(2022)**, 58, 234-236.

10. Hutter, M.; Gehring, C.; Jud, D.; Lauber, A.; Bellicoso, C.D.; Tsounis, V.; Hwangbo, J.; Bodie, K.; Fankhauser, P.; Bloesch, M. Anymal-a highly mobile and dynamic quadrupedal robot. In Proceedings of the 2016 IEEE/RSJ international conference on intelligent robots and systems (IROS), Daejeon, Korea, 9-14 October, 2016.

11. Ramezani, M.; Brandao, M.; Casseau, B.; Havoutis, I.; Fallon, M. Legged robots for autonomous inspection and monitoring of offshore assets. In Proceedings of the Offshore Technology Conference, Houston, USA, 4-7 May, 2020.

12. Zimroz, R.; Hutter, M.; Mistry, M.; Stefaniak, P.; Walas, K.; Wodecki, J. Why should inspection robots be used in deep underground mines? In Proceedings of the 27th International Symposium on Mine Planning and Equipment Selection-MPES 2018, 2019.

13. Baines, R.; Kramer-Bottiglio, R. Turtle-like robot adapts its shape and behaviour to move in different environments. *Nature* **(2022)**.

14. Tolleymichael, T.; Shepherdrobert, F.; Gallowaykevin, C.; Woodrobert, J.; Whitesidesgeorge, M. A resilient, untethered soft robot. *Soft Robot.* **(2014)**, 1, 213-223.

15. Drotman, D.; Jadhav, S.; Sharp, D.; Chan, C.; Tolley, M.T. Electronics-free pneumatic circuits for controlling soft-legged robots. *Sci. Robot.* **(2021)**, 6, eaay2627.

16. Matia, Y.; Kaiser, G.H.; Shepherd, R.F.; Gat, A.D.; Lazarus, N.; Petersen, K.H. Harnessing nonuniform pressure distributions in soft robotic actuators. *Adv. Intell. Syst.* **(2023)**, 5, 2200330.

17. Shepherd, R.F.; Ilievski, F.; Choi, W.; Morin, S.A.; Stokes, A.A.; Mazzeo, A.D.; Chen, X.; Wang, M.; Whitesides, G.M. Multigait soft robot. *Proc. Natl. Acad. Sci.* **(2011)**, 108, 20400-20403.

18. Drotman, D.; Jadhav, S.; Karimi, M.; De Zonia, P.; Tolley, M.T. 3D printed soft actuators for a legged robot capable of navigating unstructured terrain. In Proceedings of the 2017 IEEE International Conference on Robotics and Automation (ICRA), Marina Bay Sands, Singapore, 29 May - 3 June, 2017.

19. Zou, J.; Lin, Y.; Ji, C.; Yang, H. A reconfigurable omnidirectional soft robot based on caterpillar locomotion. *Soft Robot.* **(2018)**, 5, 164-174.

20. Drotman, D.; Ishida, M.; Jadhav, S.; Tolley, M.T. Application-driven design of soft, 3-D printed, pneumatic actuators with bellows. *IEEE/ASME Trans. Mechatron.* **(2018)**, 24, 78-87.

21. Yan, J.; Zhang, X.; Xu, B.; Zhao, J. A new spiral-type inflatable pure torsional soft actuator. *Soft Robot.* **(2018)**, 5, 527-540.

22. Nemiroski, A.; Shevchenko, Y.Y.; Stokes, A.A.; Unal, B.; Ainla, A.; Albert, S.; Compton, G.; Macdonald, E.; Schwab, Y.; Zellhofer, C. Arthrobots. *Soft Robot.* **(2017)**, 4, 183-190.

23. Dong, X.; Wang, Y.; Liu, X.-J.; Zhao, H. Development of modular multi-degree-of-freedom hybrid joints and robotic flexible legs via fluidic elastomer actuators. *Smart Mater. Struct.* **(2022)**, 31, 035034.

24. Sato, R.; Kazama, E.; Ming, A.; Shimojo, M.; Meng, F.; Liu, H.; Fan, X.; Chen, X.; Yu, Z.; Huang, Q. Design and control of robot legs with bi-articular muscle-tendon complex. In Proceedings of the 2017 IEEE international conference on robotics and biomimetics (ROBIO), Macao, China, 5-8 December, 2017.

25. Yamada, Y.; Nishikawa, S.; Shida, K.; Niiyama, R.; Kuniyoshi, Y. Neural-body coupling for emergent locomotion: A musculoskeletal quadruped robot with spinobulbar model. In Proceedings of the 2011 IEEE/RSJ International Conference on Intelligent Robots and Systems, San Francisco, USA, 25-30 September, 2011.

26. Verrelst, B.; Ham, R.V.; Vanderborght, B.; Daerden, F.; Lefeber, D.; Vermeulen, J. The pneumatic biped "Lucy" actuated with pleated pneumatic artificial muscles. *Auton. Robot.* **(2005)**, 18, 201-213.

27. Gorissen, B.; Milana, E.; Baeyens, A.; Broeders, E.; Christiaens, J.; Collin, K.; Reynaerts, D.; De Volder, M. Hardware sequencing of inflatable nonlinear actuators for autonomous soft robots. *Adv. Mater.* **(2019)**, 31, 1804598.

28. Tsujita, K.; Kobayashi, T.; Masuda, T. Feasibility study on stability of gait patterns with changeable body stiffness using pneumatic actuators in a quadruped robot. *Adv. Robot.* **(2009)**, 23, 503-520.

29. Tsujita, K.; Kobayashi, T.; Inoura, T.; Masuda, T. Gait transition by tuning muscle tones using pneumatic actuators in quadruped locomotion. In Proceedings of the 2008 IEEE/RSJ International Conference on Intelligent Robots and Systems, Nice, France, 22-26 September, 2008.

30. Fukuoka, Y.; Habu, Y.; Inoue, K.; Ogura, S.; Mori, Y. Autonomous speed adaptation by a muscle-driven hind leg robot modeled on a cat without intervention from brain. *Int. J. Adv. Robot. Syst.* **(2021)**, 18, 17298814211044936.

31. Fukuoka, Y.; Komatsu, R.; Machii, K.; Yokota, M.; Tobe, M.; Ibrahim, A.N.; Fukui, T.; Habu, Y. Pace Running of a Quadruped Robot Driven by Pneumatic Muscle Actuators: An Experimental Study. *Appl. Sci.* **(2022)**, 12, 4146.

32. Wait, K.W.; Goldfarb, M. A pneumatically actuated quadrupedal walking robot. *IEEE/ASME Trans. Mechatron.* **(2013)**, 19, 339-347.

33. Althoefer, K. Antagonistic actuation and stiffness control in soft inflatable robots. *Nat. Rev. Mater.* **(2018)**, 3, 76-77.

34. Yi, J.; Chen, X.; Song, C.; Zhou, J.; Liu, Y.; Liu, S.; Wang, Z. Customizable three-dimensional-printed origami soft robotic joint with effective behavior shaping for safe interactions. *IEEE Trans. Robot.* **(2018)**, 35, 114-123.

35. Tondu, B.; Ippolito, S.; Guiochet, J.; Daidie, A. A seven-degrees-of-freedom robot-arm driven by pneumatic artificial muscles for humanoid robots. *Int. J. Robot. Res.* **(2005)**, 24, 257-274.

36. Jiang, Z.; Zhang, K. A Novel Torsional Actuator Augmenting Twisting Skeleton and Artificial Muscle for Robots in Extreme Environments. In Proceedings of the 2021 IEEE International Conference on Robotics and Automation (ICRA), 2021.

37. Rong, X.; Li, Y.; Ruan, J.; Li, B. Design and simulation for a hydraulic actuated quadruped robot. *J. Mech. Sci. Technol.* **(2012)**, 26, 1171-1177.

38. Yang, K.; Li, Y.; Zhou, L.; Rong, X. Energy efficient foot trajectory of trot motion for hydraulic quadruped robot. *Energies* **(2019)**, 12, 2514.

39. Zhang, D.; Zhao, X.; Han, J. Active model-based control for pneumatic artificial muscle. *IEEE Trans. Ind. Electron.* **(2016)**, 64, 1686-1695.

40. Duong, M.-D.; Pham, Q.-T.; Vu, T.-C.; Bui, N.-T.; Dao, Q.-T. Adaptive fuzzy sliding mode control of an actuator powered by two opposing pneumatic artificial muscles. *Sci. Rep.* **(2023)**, 13, 8242.

41. Liu, G.; Sun, N.; Yang, T.; Fang, Y. Reinforcement learning-based prescribed performance motion control of pneumatic muscle actuated robotic arms with measurement noises. *IEEE Trans. Syst. Man Cybern. Syst.* **(2022)**, 53, 1801-1812.

42. Hutter, M.; Remy, C.D.; Hoepflinger, M.A.; Siegwart, R. Scarleth: Design and control of a planar running robot. In Proceedings of the 2011 IEEE/RSJ international conference on intelligent robots and systems, San Francisco, USA, 25-30 September, 2011.

43. Ruppert, F.; Badri-Spröwitz, A. Learning plastic matching of robot dynamics in closed-loop central pattern generators. *Nat. Mach. Intell.* **(2022)**, 4, 652-660.

44. Carbone, G. Stiffness analysis and experimental validation of robotic systems. *Front. Mech. Eng.* **(2011)**, 6, 182-196.

45. Vanderborght, B.; Van Ham, R.; Lefeber, D.; Sugar, T.G.; Hollander, K.W. Comparison of mechanical design and energy consumption of adaptable, passive-compliant actuators. *Int. J. Robot. Res.* **(2009)**, 28, 90-103.

46. Vuong, N.-D.; Li, R.; Chew, C.-M.; Jafari, A.; Polden, J. A novel variable stiffness mechanism with linear spring characteristic for machining operations. *Robotica* **(2017)**, 35, 1627-1637.

47. Mitsantisuk, C.; Ohishi, K.; Katsura, S. Variable mechanical stiffness control based on human stiffness estimation. In Proceedings of the 2011 IEEE International Conference on Mechatronics, 2011.

48. Zhang, L.; Li, Z.; Yang, C. Adaptive neural network based variable stiffness control of uncertain robotic systems using disturbance observer. *IEEE Trans. Ind. Electron.* **(2016)**, 64, 2236-2245.

49. Petit, F.; Albu-Schäffer, A. Cartesian impedance control for a variable stiffness robot arm. In Proceedings of the 2011 IEEE/RSJ International Conference on Intelligent Robots and Systems, 2011.

50. Jiang, Z.; Liu, C.; Zhang, K. A Variable Stiffness Continuum Parallel Manipulator With 3D Printed Pneumatic Artificial Muscles. In Proceedings of the International Design Engineering Technical Conferences and Computers and Information in Engineering Conference, 2022.

51. Hyun, D.J.; Seok, S.; Lee, J.; Kim, S. High speed trot-running: Implementation of a hierarchical controller using proprioceptive impedance control on the MIT Cheetah. *Int. J. Robot. Res.* **(2014)**, 33, 1417-1445.

52. Wensing, P.M.; Wang, A.; Seok, S.; Otten, D.; Lang, J.; Kim, S. Proprioceptive actuator design in the mit cheetah: Impact mitigation and high-bandwidth physical interaction for dynamic legged robots. *IEEE Trans. Robot.* **(2017)**, 33, 509-522.